2nd Advanced Optical Metrology Compendium

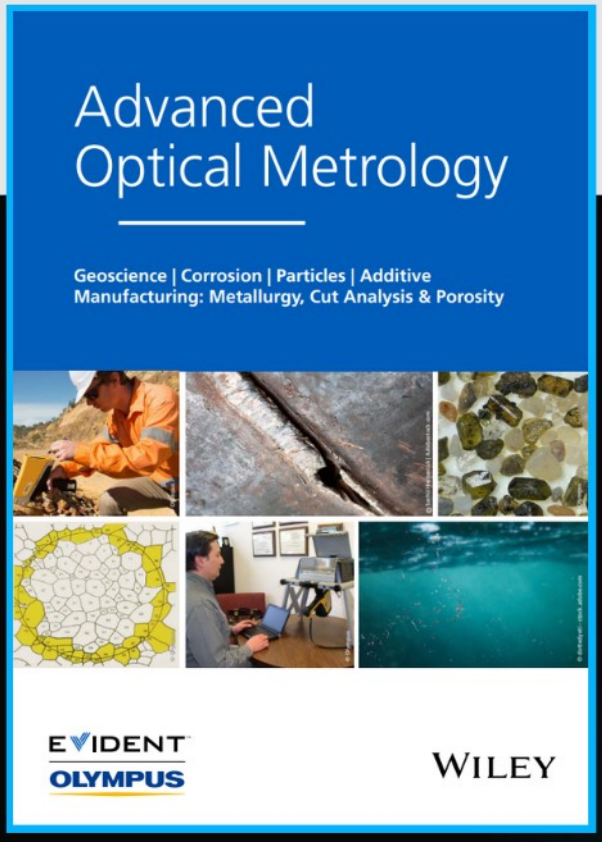

The latest eBook from Advanced Optical Metrology. Download for free.

This compendium includes a collection of optical metrology papers, a repository of teaching materials, and instructions on how to publish scientific achievements.

With the aim of improving communication between fundamental research and industrial applications in the field of optical metrology we have collected and organized existing information and made it more accessible and useful for researchers and practitioners.

EVIDENT
OLYMPUS

WILEY

NANO · MICRO small

www.small-journal.com

Interface Engineering V_2O_5 Nanofibers for High-Energy and Durable Supercapacitors

Wenchao Bi, Jichao Wang, Evan P. Jahrman, Gerald T. Seidler, Guohua Gao, Guangming Wu,* and Guozhong Cao**

A local electric field is induced to engineer the interface of vanadium pentoxide nanofibers (V_2O_5-NF) to manipulate the charge transport behavior and obtain high-energy and durable supercapacitors. The interface of V_2O_5-NF is modified with oxygen vacancies (Vö) in a one-step polymerization process of polyaniline (PANI). In the charge storage process, the local electric field deriving from the lopsided charge distribution around Vö will provide Coulombic forces to promote the charge transport in the resultant Vö-V_2O_5/PANI nanocable electrode. Furthermore, an ≈7 nm porous PANI coating serves as the external percolated charge transport pathway. As the charge transfer kinetics are synergistically enhanced by the dual modifications, Vö-V_2O_5/PANI-based supercapacitors exhibit an excellent specific capacitance (523 F g^{-1}) as well as a long cycling lifespan (110% of capacitance remained after 20 000 cycles). This work paves an effective way to promote the charge transfer kinetics of electrode materials for next-generation energy storage systems.

1. Introduction

Developing devices to store energy conveniently, controllably and sustainably is critical to solve issues of energy crisis and environmental pollution.[1] Supercapacitors have emerged as highly efficient and promising energy storage devices in intermittent renewable energy sources, smart power grids, and electrical vehicles, due to the higher power density, longer durability and safety over traditional fuel cells and batteries.[2] Great efforts have been made on elaborating the electrode materials with higher energy density for supercapacitors to meeting ever-increasing requirements. The energy density (E) of a supercapacitor is mainly dependent on the specific capacitance (C) and cell potential window (V) of electrode materials according to the equation $E = 1/2CV^2$.[3] Thus, developing electrode materials with enhanced specific capacitance is crucial for high-energy supercapacitors. Carbonaceous material based electric double-layer capacitors appear with a low capacitance due to the physical absorption/desorption at the electrode surface.[4] Comparatively, transition metal oxides (TMOs) and conductive polymers (CPs) based pseudocapacitors exhibit higher theoretical storage capacitance because of the reversible faradic reactions on or near the electrode surface.[5]

Vanadium pentoxide (V_2O_5), a layer-structured TMO, has prospective applications in electrochemical energy storage due to its high theoretical capacitance (2020 F g^{-1}), a broader operating voltage(up to ≈2.8 V), as well as low cost and abundance in nature.[6] However, the poor electrical conductivity of V_2O_5 (10^{-3} to 10^{-2} S cm^{-1}) limits the electron transfer kinetics for redox reactions. As a result, the pseudocapacitive reactions mainly occur on the surface or near-surface region of V_2O_5 electrode materials, leading to a low utilization of V_2O_5 and unsatisfactory specific capacitance.[7] In addition, the vanadium dissolution and structural instability reduces its cycling life.[8]

To address these problems, many synthetic methods have been proposed. First, nanostructured V_2O_5 materials with a large specific surface area are fabricated to provide sufficient contact area for fast Faradic reactions, such nanoribbons,[9] and nanobelts.[10] Second, tailoring the materials with multiple physicochemical properties can effectively enhance the electrochemical performance of V_2O_5 with diverse functions from components. For instance, layered V_2O_5/poly(3,4-ethylenedioxythiophene) (PEDOT)/MnO_2 nanosheets show enhanced energy density (39.2 W h kg^{-1}) and cycling stability (93.5% capacitance retention after 3000 cycles) due to the synergistic combination of PEDOT, MnO_2, and V_2O_5.[11] However, V_2O_5 electrode materials with enhanced electrochemical performance, fabricated in an uncomplicated and low-cost process are still necessary for practical applications. Based on the previous study, both polyaniline (PANI) and PEDOT improve the electrical conductivity as well as the stability of V_2O_5 by forming a conductive coating,[8,11]

W. Bi, Dr. J. Wang, Prof. G. Gao, Prof. G. Wu
Shanghai Key Laboratory of Special Artificial Microstructure Materials and Technology
School of Physics Science and Engineering
Tongji University
Shanghai 200092, China
E-mail: gao@tongji.edu.cn; wugm@tongji.edu.cn

W. Bi, Prof. G. Cao
Department of Materials Science and Engineering
University of Washington
Seattle, WA 98195-2120, USA
E-mail: gzcao@u.washington.edu

E. P. Jahrman, Prof. G. T. Seidler
Department of Physics
University of Washington
Seattle, WA 98195-1560, USA

The ORCID identification number(s) for the author(s) of this article can be found under https://doi.org/10.1002/smll.201901747.

DOI: 10.1002/smll.201901747

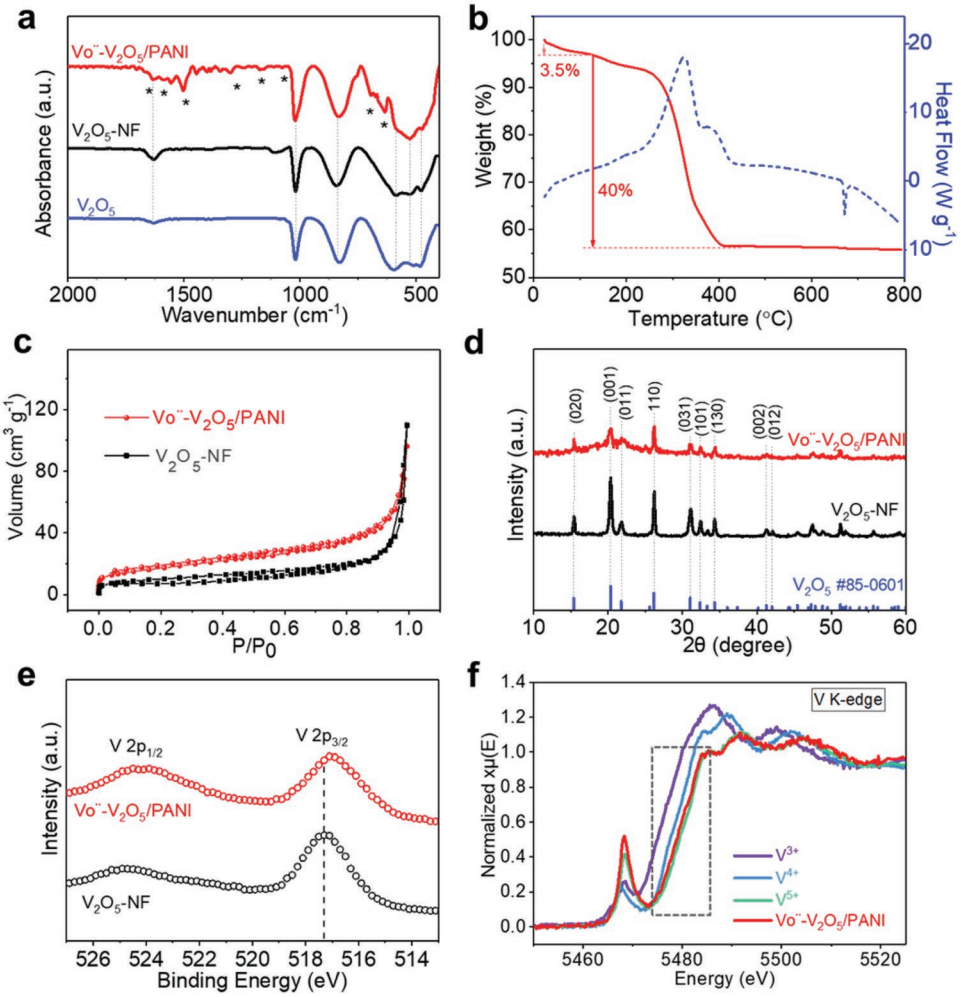

Figure 1. a) FTIR spectrum of Vö-V_2O_5/PANI, V_2O_5-NF and V_2O_5. b) TG-DSC profile of Vö-V_2O_5/PAN. c) BET surface area nitrogen adsorption-desorption isotherms and BJH pore size distributions, d) XRD patterns, and e) V 2p XPS spectra of Vö-V_2O_5/PANI and V_2O_5-NF. f) XANES analysis of Vö-V_2O_5/PANI and empirical standards. The dashed box denotes the location of the V K-edge.

while PANI has the advantage of easier preparation and lower aniline monomer cost (3.6 \$ mL^{-1}) over EDOT monomers (9.6 \$ mL^{-1}), which can be found in supporting information. Defects, especially oxygen vacancies (Vö), have been reported to intrinsically enhance the charge transfer kinetics and cycling performance of V_2O_5 by modifying its surface chemistry and electronic properties.[12] Therefore, it would be significant to improve the electrochemical performance of V_2O_5 by rationally integrating PANI and Vö into nanostructured V_2O_5 with an easy and simple method.

In this work, nanofiber-like V_2O_5 (V_2O_5-NF) are engineered with Vö and PANI at the surface region through one-step in situ oxidatively polymerization of aniline monomers. In the resultant Vö-V_2O_5/PANI nanocables, a local electric field is induced and provides Coulombic forces to promote the ion diffusion due to unbalanced charge distribution caused by Vö. The porous PANI shell offers an external percolated pathway for fast charge transport. The enlarged surface area also benefits redox reactions with a larger contact area. Thus, the charge transfer kinetics is enhanced by the interface modifications of Vö and PANI. Consequently, Vö-V_2O_5/PANI electrode manifests an excellent specific capacitance, energy density as well as a superior cycling life.

2. Results and Discussion

As shown in **Figure 1**a, the Fourier transform infrared (FTIR) spectrum of as-prepared Vö-V_2O_5/PANI shows the characteristic peaks of PANI at 1634 cm^{-1} (the stretching of quinoid rings overlaps with the band caused by structural water), 1587, 1502 (the aromatic C=C stretching, C−H in-plane bending modes), 1300 cm^{-1} (C−N stretching of secondary aromatic amine), and 692 and 633 cm^{-1} (the aromatic ring and out-of-plane deformation vibrations).[13,14] The V=O stretching bond at 1021 cm^{-1}, and V−O stretching vibration at 854 , 615, 530, and 417 m^{-1} belong to V_2O_5. The Vö-V_2O_5/PANI was further investigated by means of Raman spectrometry. As shown in Figure S2a (Supporting Information), the Raman spectrum displayed peaks of V_2O_5-NF at 146, 286, 405, 484, 528, 703, and 995 cm^{-1}, corresponding to bending vibrations of V−O−V, V=O and

bridge oxygen bonds, the stretching vibrations of chain oxygen and doubly coordinated oxygen, and in-phase stretching vibrations of V=O bonds, respectively.[29] For Vö-V_2O_5/PANI, the bands at 1240, 1349, 1403, and 1564 cm^{-1} belong to in-plane C—H bending of the benzenoid ring, C—N^+ stretching, C=C stretching of quinoid ring and benzenoid ring, indicating the existence of doped PANI in Vö-V_2O_5/PANI.[15]

Thermogravimetric and differential scanning calorimetric (TG-DSC) measurements of Vö-V_2O_5/PANI present a thermal degradation of PANI with ≈40% weight lost between 120 and 400 °C in Figure 1b.[16] An initial ≈3.5% mass loss is mainly caused by the release of adsorbed water, and the endothermic peak at around 675 °C is caused by V_2O_5.

Nitrogen sorption isotherms and pore size distributions of Vö-V_2O_5/PANI and V_2O_5-NF are shown in Figure 1c and Figure S2b (Supporting Information), respectively. Vö-V_2O_5/PANI displays a porous structure (micropores, mesopores, and macropores) with a larger specific surface area of 58 $m^2\ g^{-1}$ and V_2O_5-NF (38 $m^2\ g^{-1}$). The increase in specific surface area should be attributed to the porous PANI layer, which can serve as an external percolated pathway for charge transport in the charging and discharging process. This increased surface area is expected to provide more active sites for redox reactions, facilitating the charge storage in supercapacitors.

In the X-ray diffraction (XRD) patterns (Figure 1d), Vö-V_2O_5/PANI shows a pure V_2O_5 phase, which can be indexed to JPDS No. 85-0601. Compared with V_2O_5-NF, the decreased peak intensity of Vö-V_2O_5/PANI suggests lower crystallinity degree in Vö-V_2O_5/PANI, which could be caused by Vö and PANI.

Figure 1e presents the V 2p X-ray photoelectron spectroscopy (XPS) spectra of Vö-V_2O_5/PANI with two main peaks of V $2p_{1/2}$ and V $2p_{3/2}$ at ≈524.4 and ≈517.1 eV, respectively. Compared with V_2O_5-NF, the peaks of Vö-V_2O_5/PANI shift to lower binding energies, which suggests the existence of low oxidation states of vanadium. The decomposition of V $2p_{3/2}$ spectra reveals the percentage of V^{3+} and V^{4+} in Vö-V_2O_5/PANI (49.7%) is larger than in V_2O_5-NF (8.8%), and the average oxidation state of vanadium in Vö-V_2O_5/PANI decreases to 4.6, as shown in Figure S3 (Supporting Information). Based on the XRD result that Vö-V_2O_5/PANI demonstrates a pure V_2O_5 phase, it can be concluded that V^{3+} and V^{4+} are related to Vö, which engineer the surface of V_2O_5-NF.

For further study, X-ray absorption near-edge structure (XANES) measurements were employed to probe the oxidation states of vanadium in Vö-V_2O_5/PANI in bulk, and the commercial V_2O_3, VO_2 and V_2O_5 served as empirical standards.[17] In Figure 1f, the V K-edge XANES spectrum of Vö-V_2O_5/PANI presents a modest edge shift to lower photon energies, which corresponds to reduction of the system and suggests the existence of Vö in Vö-V_2O_5/PANI. In addition, the spectrum of Vö-V_2O_5/PANI generally agrees with that of V^{5+}, which reveals the bulk of V atoms remain in V^{5+}. The fitting result show a smaller concentration of Vö (5.4 %) than XPS result (49.7%), confirming the near-surface engineering of Vö in Vö-V_2O_5/PANI. This result is also consistent with XPS and XRD results.

Scanning electron microscopy (SEM) images shows a porous and nanofiber-like structure of Vö-V_2O_5/PANI in **Figure 2**a,b. Transmission electron microscopy (TEM) images display a nanocable structure with an ≈7 nm uniform PANI shell, as shown in Figure 2c,d. High-resolution TEM (HRTEM) image (Figure 2e) demonstrates defects with blurred lattice fringes and dark points. After further characterized by inverse fast Fourier transform (IFFT) in Figure 2f,g, dislocations are observed in red circles, accompanied with an expanded interplanar spacing ranging from 5.94 to 6.79 Å (standard parameter is 5.76 Å), corresponding to the (020) crystal planes of V_2O_5. These dislocations arise from Vö which induce the skewing of other vanadium atoms around the vacancy sites in V_2O_5. These dislocations not only show obvious evidence of the generation of Vö in Vö-V_2O_5/PANI, but also agree with the above XRD, XPS and XANES results. Vö help to ensure the uniformity of PANI by providing favorable nucleation sites for the polymerization of PANI monomers, limiting the mobility of monomers and restricting the formation and the aggregation of PANI nanoparticles during the polymerization processes, which is also proved in Vö-modified CoO_3/graphene.[18] The uniformity of PANI is further proven by energy-dispersive X-ray spectrometry (EDS) mapping analysis (Figure 2h) and line scan profile (Figure 2i) from high-angle annular dark-field scanning transmission electron microscopy (HADDF-STEM). Based on all the results, the interface of Vö-V_2O_5/PANI is simultaneously engineered with Vö and porous PANI coating.

In the polymerization process of PANI, aniline monomers are oxidized and involve electron lost and deprotonation process.[19] As is known that electron can be taken away from oxygen (O_o^x) in V_2O_5 primitive lattice and then generate Vö and O″, O″ and H^+ will form H_2O, and V_v^x in V_2O_5 receives these electrons and obtain V^{4+} and even V^{3+}. Therefore, the possible reactions are believed to proceed as follows (Equations (1)–(4))

$$n\,C_6H_5NH_2-(2n-2)e'\rightarrow H(C_6H_4NH)_n\,H+(2n-2)\,H^+ \quad (1)$$

$$O_o^x=V\ddot{o}+O'' \quad (2)$$

$$2H^++O''\rightarrow H_2O(g) \quad (3)$$

$$V_v^x+e'\rightarrow V_v' \quad (4)$$

$$V_v'+e'\rightarrow V_v'' \quad (5)$$

The above reactions can be written as follows

$$nC_6H_5NH_2+(2n-2)\,V_v^x+(n-1)\,O_o^x\rightarrow H(C_6H_4NH)_nH +mV_v'+\left(n-1-\frac{1}{2}m\right)V_v''+(n-1)\,V\ddot{o}+(n-1)\,H_2O(g) \quad (6)$$

The cyclic voltammetry (CV) and galvanostatic charge/discharge (GCD) measurements were carried out to evaluate the electrochemical potential of Vö-V_2O_5/PANI in a symmetric supercapacitor. The electrolyte is 1 M Na_2SO_4 aqueous solution. Vö-V_2O_5/PANI electrodes show pseudocapacitive behaviors with rectangular-like CV loops (**Figure 3**a) and symmetric GCD curves (Figure 3b) under different scan rates. No redox peaks are observed because that the fast, reversible, successive multiple redox reactions occur at the electrode surface.[20] The specific capacitance of Vö-V_2O_5/PANI electrode is 523 F g^{-1} when the current density is 0.5 A g^{-1}. Such an excellent specific

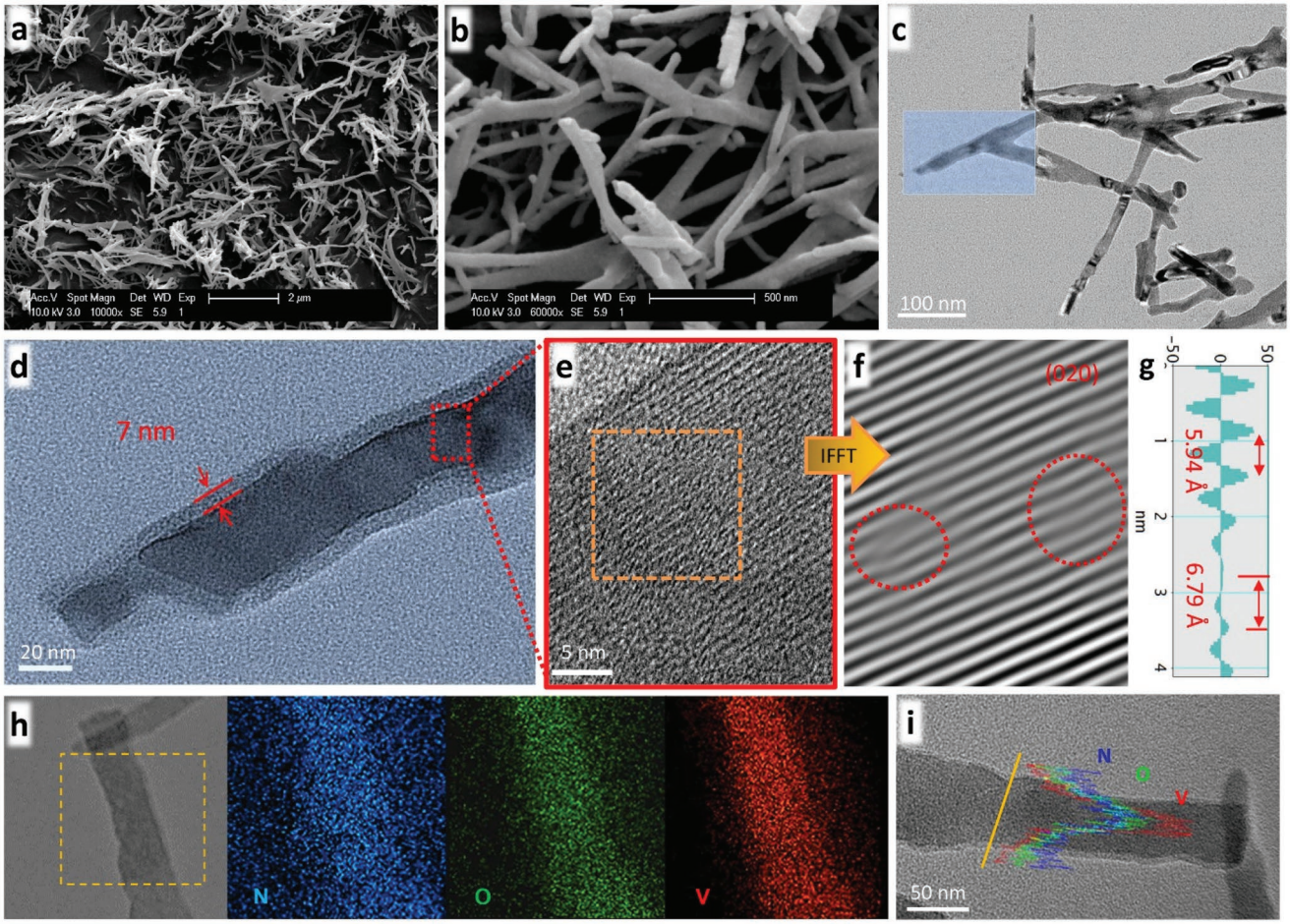

Figure 2. a,b) SEM images, c,d) TEM images, and e) HRTEM image of Vö-V_2O_5/PANI of the selected area in (d). f,g) IFFT image and corresponding line profile of (e). h) TEM-EDS element mappings and i) line scanning profile of Vö-V_2O_5/PANI.

capacitance can be attributed to the addition of Vö as well as the porous PANI shell in V_2O_5. For further study, V_2O_5-NF and commercial PANI (Alfa Aesar) were mechanically mixed (noted as V_2O_5/PANI) with the mass ratio from the TG-DSC result, since Vö and PANI are simultaneously introduced into V_2O_5. Detail information can be found in Figure S4 (Supporting Information). As shown in Figure 3c, the voltammogram area (5 mV s^{-1}) of V_2O_5/PANI (without Vö) is between Vö-V_2O_5/PANI and V_2O_5-NF due to the PANI. Consistently, the specific capacitance of V_2O_5/PANI (316 F g^{-1}) is much lower than that of Vö-V_2O_5/PANI (523 F g^{-1}), higher than that of V_2O_5-NF (225 F g^{-1}) at 0.5 A g^{-1} in Figure 3d. The above results directly evidence that the excellent electrochemical performance of Vö-V_2O_5/PANI results from the synergy between Vö and PANI. Vö-V_2O_5/PANI electrodes deliver a higher specific capacitance than V_2O_5/PANI and V_2O_5-NF even at large current density of 10 A g^{-1}, as shown in Figure 3e. In Figure 3f, the energy density of Vö-V_2O_5/PANI is 73 W h kg^{-1}, higher than that of V_2O_5/PANI (44 W h kg^{-1}) and V_2O_5-NF (31 W h kg^{-1}), when the power density is 2500 W kg^{-1}.

As the terminally (vanadyl) oxygen has been reported as the easiest site to generate Vö in V_2O_5 bulk structure,[21] the following discussion will focus on the Vö located at a vanadyl bound oxygen. The Vö site viewed along different directions are shown in **Figure 4**a. With skewing of vanadium atoms, especially around the Vö sites, which was obviously observed as dislocations in the above IFFT images, an imbalanced charge distribution would occur in V_2O_5 layer plane, resulting in a positive region in the Vö center and a corresponding negatively charged region around Vö. As illustrated in Figure 4b, when discharging, an adventitious electric field forms with the direction from the non-Vö area to the negatively charged region, and the Coulombic force will attract Na^+ ions to migrate to the area around the Vö. Then, the negatively charged area will be electrically neutral after fully discharged. When charging, the Na^+ migration will be accelerated by the Coulombic force from the local electric field, whose direction is from the positive region of the Vö center to the neutral Na^+ area. Thus, the ion transfer dynamics is promoted by the Vö caused local electric field, which is also founded in other layer-structure electrode materials.[22]

In the Nyquist plots in Figure 4d, Vö-V_2O_5/PANI electrode manifests a much smaller electron transfer resistance *Rct* (3.2 Ω) than V_2O_5/PANI (14.1 Ω) and V_2O_5-NF (18.9 Ω), and Vö-V_2O_5/PANI exhibits the largest slope, which suggests enhanced electron transfer kinetics and faster ion diffusion in

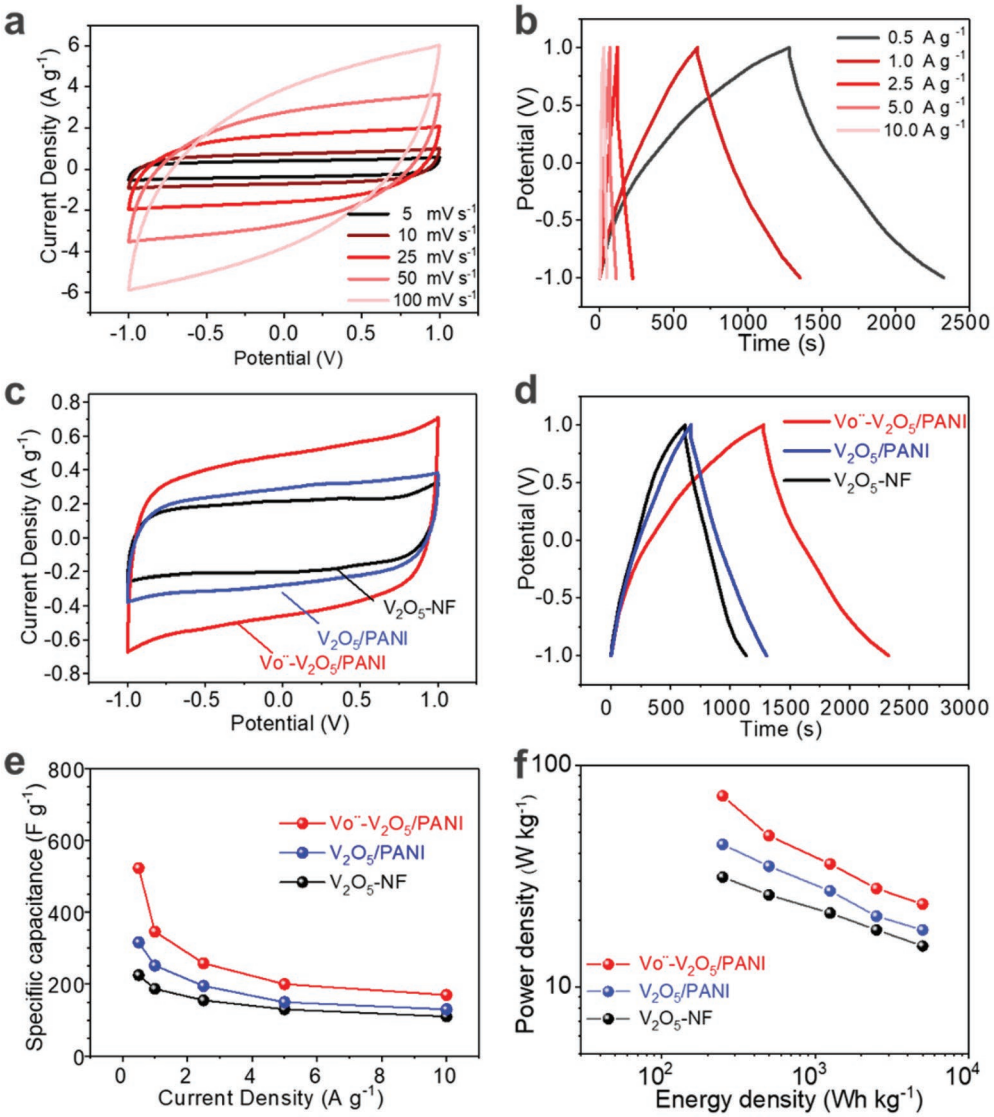

Figure 3. a) CV curves, b) GCD curves of Vö-V_2O_5/PANI under different scan rates, c) CV curves at 5 mV s^{-1}, d) GCD curves at 0.5 A g^{-1}, e) specific capacitances, and f) Ragone plots of Vö-V_2O_5/PANI, mechanically mixed V_2O_5/PANI- and V_2O_5-NF-based supercapacitors.

Vö-V_2O_5/PANI for redox reactions. This enhancement renders Vö-V_2O_5/PANI excellent electrochemical performance. It is worth noting that, the resistance of V_2O_5/PANI electrode get larger than Vö-V_2O_5/PANI without Vö, while much improved by PANI compared with V_2O_5-NF. Thus, the high electrochemical performance of Vö-V_2O_5/PANI derives from synergistically enhanced kinetics by both rich Vö in the surface of V_2O_5 and the electronically conductive porous PANI coating. As schematically illustrated in Figure 4c, not only do Vö enable fast electron transfer by providing void sites for electron acceptance/donation, but also catalyze the redox reaction at the surface.[12] The expanded interplanar spacing also provide an efficient channel for ionic transport. Moreover, Vö promote the Na^+ ion transfer dynamics with an adventitious Coulombic force by intrinsically inducing a local electric field in the plane of V_2O_5 (analyzed above). On the other hand, the porous PANI shell serves as the external percolated charge transport pathway in a nanocable nanostructure and accelerate the electron transfer due to its high electrical conductivity.[16]

In Figure 4e, Vö-V_2O_5/PANI electrode delivers 110% of the initial capacitance retention after 20 000 cycles at 10 A g^{-1}, accompanied with a Coulombic efficiency of nearly 100%. The corresponding GCD curves of the first 5 cycles and the last 5 cycles suggest no capacitance degradation after cycling. SEM and TEM images (Figure S5a–c, Supporting Information) display a well-preserved nanocable structure for Vö-V_2O_5/PANI electrode after cycling. In HRTEM image (Figure S5d, Supporting Information), although the PANI shell changes slightly with the thickness ranging from ≈4 to ≈7 nm, the PANI coating remains tightly anchored to V_2O_5-NF due to the in situ polymerization of PANI, which proves the excellent structural integrity and stability of Vö-V_2O_5/PANI; the long cycling durability is attributed to the following. First, the porous PANI shell enhances the charge transfer kinetics by providing external

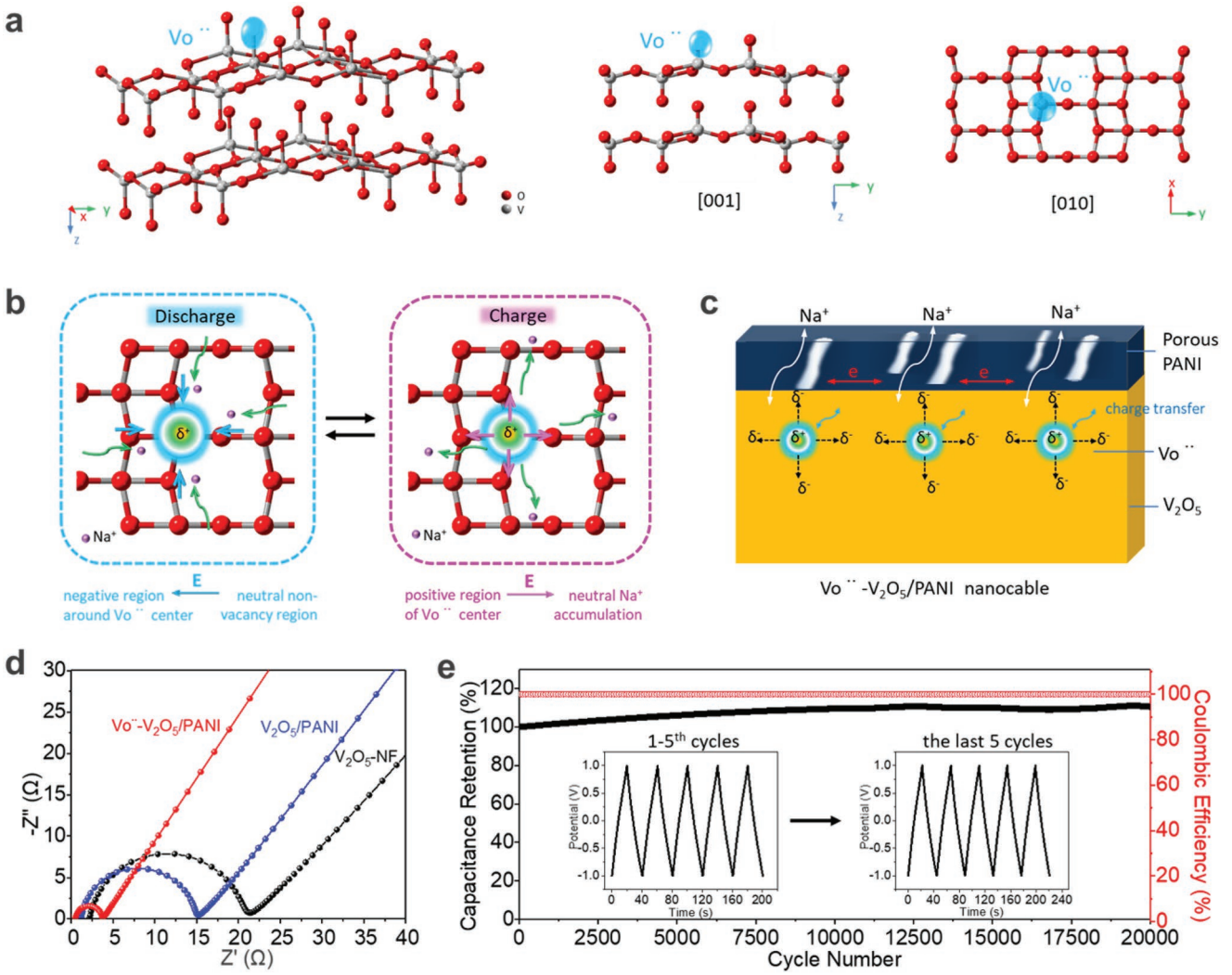

Figure 4. a) The vacancy site in V_2O_5 structure viewed along the [001] and [010] directions. b) Schematic illustration of charge transfer behavior around the Vö region by forming local electric field (*E*). c) The enhanced charge transfer kinetics mechanism of Vö-V_2O_5/PANI due to the synergy of Vö and PANI. d) Nyquist plots of Vö-V_2O_5/PANI, mechanically mixed V_2O_5/PANI and V_2O_5-NF based supercapacitors. e) Cycling performance and corresponding Coulombic efficiency of Vö-V_2O_5/PANI at 10 A g^{-1} (inset shows the first 5 and the last 5 GCD curves at 10 A g^{-1}).

percolated charge transport pathway and enlarging the surface area for high utilization of active materials, similar results have also been reported in literature.[23] PANI coating may also prevent or retard vanadium dissolution into electrolyte, and buffers the volume expansion/contraction of V_2O_5 during charge/discharge process, as suggested in literature[8,24] The above advantages of PANI are beneficial for the structural stability of V_2O_5. Second, Vö can balance the internal stress and electrostatic repulsion of adjacent layers, stabilizing the layer structure of V_2O_5.[25] For the increasing capacitance, with Vö distributed at the surface of V_2O_5-NF, the electric field for charging/discharging may promote Vö to migrate and diffuse, leading to more V^{5+} at the surface region for redox reactions.[26] It is also possible that Vö-V_2O_5/PANI are electro-activated by electrolyte and then results in an increased specific capacitance after a long time of cycling.[33] This cyclability is superior to other supercapacitors based on V_2O_5/PANI nanowires (92% after 5000 cycles),[14] V_2O_5/graphene/MWCNT (82.9% after 32 500 cycles),[29] V_2O_5/PPy network (81% after 1000 cycles),[27] and core-shell V_2O_5/PPy (82.7% after 2000 cycles).[28]

3. Conclusions

Local electric field has been induced in the shallow layer of Vö-V_2O_5/PANI nanocables in a one-step oxidative polymerization process. In the resultant Vö-V_2O_5/PANI nanocables, caused by a lopsided charge distribution around Vö, the local electric field provides Coulombic forces to promote charge transport of in V_2O_5-NF. Simultaneously, the ≈7 nm porous PANI layer serves as external percolated transport pathway for charge during the charging and discharging processes. Therefore, charge transfer dynamics of Vö-V_2O_5/PANI electrode is synergistically enhanced by Vö and porous PANI shells, resulting in an excellent specific capacitance at 523 F g^{-1} and a high energy density of 73 W h kg^{-1} at the power density of

2500 W kg^{-1}. Vö-V_2O_5/PANI show a long cycling life with 110% of initial capacitance remained after 20 000 cycles. This work paves an effective way to enhance the electrochemical properties of transmission metal oxides for next-generation energy storage devices.

4. Experimental Section

Synthesis of V_2O_5-NF: V_2O_5-NF was prepared with the same method as reported.[29] Briefly, V_2O_5 powder, benzyl alcohol and isopropanol (a molar ratio of 1:4:40) were admixed and kept at 90 °C under condensate reflux for 4 h. After filtration, the filtrate was concentrated to 1/3 volume by heating reflux at 110 °C. Then, 10 mL deionized water was added into 15 mL above vanadium oxide oligomers under vigorous stirring and kept at 50 °C for 2 days. After solvent replacement, freeze drying and heating in air at 300 °C for 3 h, V_2O_5-NF was obtained.

Synthesis of Vö-V_2O_5/PANI nanocables: V_2O_5-NF was pretreated with hydrochloric acid (36 wt%, 0.5 mL) in vacuum in 25 °C. 0.5 mL aniline monomers was used and vapored aniline monomers deposited and polymerized on the surface of V_2O_5-NF at 80 °C in vacuum, generating Vö in the shallow layer of V_2O_5-NF and forming a PANI coating. The sample was dried in 120 °C in vacuum for 12 h. The yellow V_2O_5-NF turns dark blue (Figure S1, Supporting Information), which indicates the successful fabrication of Vö-V_2O_5/PANI.

Chemical and Structural Characterizations: The composition of samples was identified with Fourier transform infrared spectroscopy (Bruker-TENSOR27 FTIR spectrometer) from 400 to 4000 cm^{-1}, and with Thermogravimetric and differential scanning calorimetry analyses on SDT Q600 from 25 to 800 °C, at a heating rate of 10 °C min^{-1} (flowing air). Nitrogen adsorption isotherms were conducted on an Autosorb-1 (Quantachorme) analyzer. The crystalline information of as-prepared samples was measured by X-ray diffractometer (Bruker D8 Advance, Germany) using a Rigaku D/max-C diffractometer and Cu Kα (λ = 0.15406 nm) radiation. The surficial vanadium oxidation states of all sample were examined by X-ray photoelectron spectroscopy and the spectrum was obtained with Mg Kα radiation ($h\nu$ = 1253.6 eV) in the PHI-5,000C ESCA system. The concentration of each oxidation state of vanadium cations was estimated from the corresponding peak area percentage. The overall vanadium oxidation states of the samples were examined by X-ray absorption near-edge structure measurements in the vanadium K-edge using laboratory-based instrumentation (University of Washington),[30] and analyzed with a reported methodology.[31] Fitting was performed in Mathematica with the energy from 5460 to 5490 eV, using the function NonlinearModelFit through a linear combination of the spectra of reference compounds. The fitting was constrained that the component of each oxide compound be between null and unity and the sum of all components be unity. The morphologies of all samples were characterized by field emission scanning electron microscopy (FESEM, S-4800, Japan) and transmission electron microscopy (JEOLR2100, Japan). Raman spectra (Jobin-Yvon HR800) were recorded from 100 to 2000 cm^{-1} using a 514 nm argon ion laser.

Electrochemical Characterizations: The electrodes were prepared by mixing active materials, acetylene black and poly(vinylidene fluoride) (PVDF) in *N*-methylpyrrolidone (NMP) with a mass ratio of 80:10:10. The slurry was painted onto a graphite paper current collector and dried under vacuum at 120 °C overnight. A symmetric-electrode test cell and 1 M Na_2SO_4 solution were used. Mass loading of each electrode is about 1 mg cm^{-2}. Cyclic voltammogram and galvanostatic charge/discharge and electrochemical impedance spectroscopy (EIS) were performed on a CHI660C (Chenhua) electrochemical working station with the voltage from −1 to 1 V.[10,32,33] The scan rates of CV are 5, 10, 25, 50, and 100 mV s^{-1}, and the current densities of GCD are 0.5, 1, 2.5, 5, and 10 A g^{-1}. The EIS was carried out in the frequency range 0.01 Hz to 100 kHz with an AC voltage amplitude of 5 mV. The specific capacitance of each electrode (C, F g^{-1}) was calculated from the discharging process in GCD curves according to the equation $C = I\Delta t/(m\Delta V)$, where I is the constant discharging current, m is the total mass of each electrode, Δt is the discharging duration, and ΔV is the voltage window (1 V). The equations of $E = (1/2)C(\Delta V)^2/3600$ and $P = E/\Delta t$ were used to calculate energy density (E, W h kg^{-1}) and power density (P, W kg^{-1}) in Ragone plots, respectively.[34]

Supporting Information

Supporting Information is available from the Wiley Online Library or from the author.

Acknowledgements

The work was supported financially in part by the National Natural Science Foundation of China (Grant Nos. U1503292 and 51872204), the Fundamental Research Funds for the Central Universities, and the National Key Research and Development Program of China (Grant No. 2017YFA0204600). This work was also supported by the National Science Foundation (1803256). W.C.B. was supported by the China Scholarship Council (CSC) for studying at the University of Washington. E.P.J. was supported by a subcontract from the National Institute of Standards and Technology. Opinions, recommendations, findings, and conclusions presented in this manuscript and associated materials do not necessarily reflect the views or policies of NIST or the United States Government.

Conflict of Interest

The authors declare no conflict of interest.

Keywords

interfaces, local electric fields, polyaniline, supercapacitors, vanadium pentoxide

Received: April 5, 2019
Revised: May 21, 2019
Published online: June 19, 2019

[1] a) Y. Wang, X. Fu, M. Zheng, W. H. Zhong, G. Cao, *Adv. Mater.* **2019**, *31*, 1804204; b) S. Chu, A. Majumdar, *Nature* **2012**, *488*, 294; c) X. Zhao, H.-E. Wang, R. C. Massé, J. Cao, J. Sui, J. Li, W. Cai, G. Cao, *J. Mater. Chem. A* **2017**, *5*, 7394; d) G. Fang, J. Zhou, A. Pan, S. Liang, *ACS Energy Lett.* **2018**, *3*, 2480; e) L. Yu, X. Y. Yu, X. W. D. Lou, *Adv. Mater.* **2018**, *30*, 1800939.

[2] a) X. Zhao, W. Cai, Y. Yang, X. Song, Z. Neale, H.-E. Wang, J. Sui, G. Cao, *Nano Energy* **2018**, *47*, 224; b) Y. Wang, Y. Zhang, J. Shi, X. Kong, X. Cao, S. Liang, G. Cao, A. Pan, *Energy Storage Mater.* **2019**, *18*, 366; c) Y. Wang, Z. Nie, A. Pan, Y. Zhang, X. Kong, T. Zhu, S. Liang, G. Cao, *J. Mater. Chem. A* **2018**, *6*, 6792.

[3] a) Y. Wang, Y. Song, Y. Xia, *Chem. Soc. Rev.* **2016**, *45*, 5925; b) P. Ratajczak, M. E. Suss, F. Kaasik, F. Béguin, *Energy Storage Mater.* **2019**, *16*, 126; c) D. Liu, Q. Li, S. Li, J. Hou, H. Zhao, *Nanoscale* **2019**, *11*, 4362.

[4] a) Q. Ma, Y. Yu, M. Sindoro, A. G. Fane, R. Wang, H. Zhang, *Adv. Mater.* **2017**, *29*; b) V. Sahu, S. Shekhar, R. K. Sharma, G. Singh, *ACS Appl. Mater. Interfaces* **2015**, *7*, 3110.

[5] a) F. Wang, X. Wu, X. Yuan, Z. Liu, Y. Zhang, L. Fu, Y. Zhu, Q. Zhou, Y. Wu, W. Huang, *Chem. Soc. Rev.* **2017**, *46*, 6816; b) L.-b. Jiang,

X.-z. Yuan, J. Liang, J. Zhang, H. Wang, G.-m. Zeng, *J. Power Sources* **2016**, *331*, 408; c) M. Gao, W. K. Wang, Q. Rong, J. Jiang, Y. J. Zhang, H. Q. Yu, *ACS Appl. Mater. Interfaces* **2018**, *10*, 23163.
[6] a) Y. Wang, G. Z. Cao, *Chem. Mater.* **2006**, *18*, 2787; b) M. Ghosh, V. Vijayakumar, R. Soni, S. Kurungot, *Nanoscale* **2018**, *10*, 8741; c) R. Qi, J. Nie, M. Liu, M. Xia, X. Lu, *Nanoscale* **2018**, *10*, 7719.
[7] Y. Yan, B. Li, W. Guo, H. Pang, H. Xue, *J. Power Sources* **2016**, *329*, 148.
[8] Z. Tong, S. Liu, X. Li, Y. Ding, J. Zhao, Y. Li, *Electrochim. Acta* **2016**, *222*, 194.
[9] L. J. Cao, J. X. Zhu, Y. H. Li, P. Xiao, Y. H. Zhang, S. T. Zhang, S. B. Yang, *J. Mater. Chem. A* **2014**, *2*, 13136.
[10] J. X. Zhu, L. J. Cao, Y. S. Wu, Y. J. Gong, Z. Liu, H. E. Hoster, Y. H. Zhang, S. T. Zhang, S. B. Yang, Q. Y. Yan, P. M. Ajayan, R. Vajtai, *Nano Lett.* **2013**, *13*, 5408.
[11] C. X. Guo, G. Yilmaz, S. Chen, S. Chen, X. Lu, *Nano Energy* **2015**, *12*, 76.
[12] H. Song, C. Liu, C. Zhang, G. Cao, *Nano Energy* **2016**, *22*, 1.
[13] I. Šeděnková, M. Trchová, J. Stejskal, *Polym. Degrad. Stab.* **2008**, *93*, 2147.
[14] M. H. Bai, T. Y. Liu, F. Luan, Y. Li, X.-X. Liu, *J. Mater. Chem. A* **2014**, *2*, 10882.
[15] a) T. K. Gupta, B. P. Singh, R. B. Mathur, S. R. Dhakate, *Nanoscale* **2014**, *6*, 842; b) L. Jin, Y. Jiang, M. Zhang, H. Li, L. Xiao, M. Li, Y. Ao, *Sci. Rep.* **2018**, *8*, 6268.
[16] N. Asim, S. Radiman, M. A. b. Yarmo, *Mater. Lett.* **2008**, *62*, 1044.
[17] W. Bi, Y. Wu, C. Liu, J. Wang, Y. Du, G. Gao, G. Wu, G. Cao, *ACS Appl. Energy Mater.* **2019**, *2*, 668.
[18] S. Yang, Y. Liu, Y. Hao, X. Yang, W. A. Goddard III, X. L. Zhang, B. Cao, *Adv. Sci.* **2018**, *5*, 1700659.
[19] A. T. Lawal, G. G. Wallace, *Talanta* **2014**, *119*, 133.
[20] a) P. Simon, Y. Gogotsi, *Nat. Mater.* **2008**, *7*, 845; b) K. Zheng, Y. Zeng, S. Liu, C. Zeng, Y. Tong, Z. Zheng, T. Zhu, X. Lu, *Energy Storage Mater.* **2019**, https://doi.org/10.1016/j.ensm.2019.02.012.
[21] D. O. Scanlon, A. Walsh, B. J. Morgan, G. W. Watson, *J. Phys. Chem. C* **2008**, *112*, 9903.
[22] a) Y. Liu, T. Zhou, Y. Zheng, Z. He, C. Xiao, W. K. Pang, W. Tong, Y. Zou, B. Pan, Z. Guo, Y. Xie, *ACS Nano* **2017**, *11*, 8519; b) Y. Zheng, T. Zhou, X. Zhao, W. K. Pang, H. Gao, S. Li, Z. Zhou, H. Liu, Z. Guo, *Adv. Mater.* **2017**, *29*, 1700396.
[23] a) L. Dong, G. Liang, C. Xu, D. Ren, J. Wang, Z.-Z. Pan, B. Li, F. Kang, Q.-H. Yang, *J. Mater. Chem. A* **2017**, *5*, 19934; b) L. Dong, G. Liang, C. Xu, W. Liu, Z.-Z. Pan, E. Zhou, F. Kang, Q.-H. Yang, *Nano Energy* **2017**, *34*, 242.
[24] a) Q. T. Qu, Y. S. Zhu, X. W. Gao, Y. Wu, *Adv. Energy Mater.* **2012**, *2*, 950; b) W. Liu, N. Liu, Y. Shi, Y. Chen, C. Yang, J. Tao, S. Wang, Y. Wang, J. Su, L. Li, Y. Gao, *J. Mater. Chem. A* **2015**, *3*, 13461.
[25] T. Zhai, S. Xie, M. Yu, P. Fang, C. Liang, X. Lu, Y. Tong, *Nano Energy* **2014**, *8*, 255.
[26] a) Y. Xu, M. Zhou, C. Zhang, C. Wang, L. Liang, Y. Fang, M. Wu, L. Cheng, Y. Lei, *Nano Energy* **2017**, *38*, 304; b) Y. Li, Y. Lei, B. G. Shen, J. R. Sun, *Sci. Rep.* **2015**, *5*, 14576.
[27] T. Qian, N. Xu, J. Q. Zhou, T. Z. Yang, X. J. Liu, X. W. Shen, J. Q. Liang, C. L. Yan, *J. Mater. Chem. A* **2015**, *3*, 488.
[28] J. G. Wang, H. Liu, H. Liu, W. Hua, M. Shao, *ACS Appl. Mater. Interfaces* **2018**, *10*, 18816.
[29] W. Bi, G. Gao, Y. Wu, H. Yang, J. Wang, Y. Zhang, X. Liang, Y. Liu, G. Wu, *RSC Adv.* **2017**, *7*, 7179.
[30] a) E. P. Jahrman, W. M. Holden, A. S. Ditter, D. R. Mortensen, G. T. Seidler, T. T. Fister, S. A. Kozimor, L. F. J. Piper, J. Rana, N. C. Hyatt, M. C. Stennett, *Rev. Sci. Instrum.* **2019**, *90*, 024106; b) G. T. Seidler, D. R. Mortensen, A. J. Remesnik, J. I. Pacold, N. A. Ball, N. Barry, M. Styczinski, O. R. Hoidn, *Rev. Sci. Instrum.* **2014**, *85*, 113906.
[31] W. Bi, E. P. Jahrman, G. T. Seidler, J. Wang, G. Gao, G. Wu, M. Atif, M. S. AlSalhi, G. Cao, *ACS Appl. Mater. Interfaces* **2019**, *11*, 16647.
[32] Y. J. Wu, G. H. Gao, G. M. Wu, *J. Mater. Chem. A* **2015**, *3*, 1828.
[33] Y. J. Wu, G. H. Gao, H. Y. Yang, W. Bi, X. Liang, Y. Zhang, G. Zhang, G. Wu, *J. Mater. Chem. A* **2015**, *3*, 15692.
[34] J. W. Park, W. Na, J. Jang, *J. Mater. Chem. A* **2016**, *4*, 8263.